

1 A numerical model study of the main factors contributing to
2 hypoxia and its interannual and intra-seasonal variability off the
3 Changjiang Estuary

4
5 Haiyan Zhang^{1,2}, Katja Fennel^{1,*}, Arnaud Laurent¹, Changwei Bian³

6
7 ¹Department of Oceanography, Dalhousie University, Halifax, Nova Scotia, Canada

8 ²School of Marine Science and Technology, Tianjin University, Tianjin, China

9 ³Physical Oceanography Laboratory/CIMST, Ocean University of China, and Qingdao
10 National Laboratory for Marine Science and Technology, Qingdao, China

11 *Corresponding author

12 **Abstract**

13 A three-dimensional physical-biological model of the marginal seas of China was used
14 to analyze interannual and intra-seasonal variations in hypoxic conditions and identify the
15 main processes controlling their generation off the Changjiang Estuary. The model was
16 compared against available observations and reproduces the observed temporal and spatial
17 variability of physical and biological properties including bottom oxygen. Interannual
18 variations of hypoxic extent in the simulation are partly explained by variations in river
19 discharge but not nutrient load. As riverine inputs of freshwater and nutrients are
20 consistently high, promoting large productivity and subsequent oxygen consumption in the
21 region affected by the river plume, wind forcing is important in modulating interannual and
22 intra-seasonal variability. Wind direction is relevant because it determines the spatial extent
23 and distribution of the freshwater plume which is strongly affected by either upwelling or
24 downwelling conditions. High-wind events can lead to partial reoxygenation of bottom
25 waters and, when occurring in succession throughout the hypoxic season, can effectively
26 suppress the development of hypoxic conditions thus influencing interannual variability.
27 An oxygen budget is presented and shows that sediment oxygen consumption is the
28 dominant oxygen sink below the pycnocline and that advection of oxygen in the bottom
29 waters acts as an oxygen sink in spring but becomes a source during hypoxic conditions in

30 summer especially in the southern part of the hypoxic region, which is influenced by open-
31 ocean intrusions.

32

33 **1. Introduction**

34 In coastal seas, hypoxic conditions (oxygen concentrations lower than 2 mg L⁻¹ or 62.5
35 mmol m⁻³) are increasingly caused by rising anthropogenic nutrient loads from land (Diaz
36 & Rosenberg, 2008; Rabalais et al., 2010; Fennel and Testa, 2019). Hypoxic conditions are
37 detrimental to coastal ecosystems leading to a decrease in species diversity and rendering
38 these systems less resilient (Baird et al., 2004; Bishop et al., 2006; Wu, 2002). Hypoxia is
39 especially prevalent in coastal systems influenced by major rivers such as the northern Gulf
40 of Mexico (Bianchi et al., 2010), Chesapeake Bay (Li et al., 2016), and the Changjiang
41 Estuary (CE) in the East China Sea (Li et al., 2002).

42 The Changjiang is the largest river in China and fifth largest in the world in terms of
43 volume transport, with an annual discharge of 9×10^{11} m³ year⁻¹ via its estuary (Liu et al.,
44 2003). The mouth of the CE is at the confluence of the southeastward Yellow Sea Coastal
45 Current and the northward Taiwan Warm Current (Figure 1). Hydrographic properties in
46 the outflow region of the CE are influenced by several different water masses including
47 fresh Changjiang Diluted Water, relatively low-salinity coastal water, more saline water
48 from the Taiwan Warm Current, and high-nutrient, low-oxygen water from the subsurface
49 of the Kuroshio (Wei et al., 2015; Yuan et al., 2008). The interactions of these water masses
50 together with wind forcing and tidal effects lead to a complicated and dynamic environment.

51 Freshwater (FW) discharge by the Changjiang reaches its minimum in winter when the
52 strong northerly monsoon (dry season) prevails and peaks in summer during the weak
53 southerly monsoon (wet season) resulting in a large FW plume adjacent to the estuary.
54 Along with the FW, the Changjiang delivers large quantities of nutrients to the East China
55 Sea (ECS) resulting in eutrophication in the plume region (Li et al., 2014; Wang et al.,
56 2016). Since the 1970s, nutrient load has increased more than twofold with a subsequent
57 increase in primary production (PP) in the outflow region of the estuary (Liu et al., 2015).
58 Hypoxia off the CE was first detected in 1959 and, with a spatial extent of up to 15,000
59 km², is among the largest coastal hypoxic zones in the world (Fennel & Testa, 2019).
60 Although no conclusive trend in oxygen minima has been observed (Wang, 2009; Zhu et

61 al., 2011), hypoxic conditions are suspected to have expanded and intensified in recent
62 decades (Li et al., 2011; Ning et al., 2011) due to the increasing nutrient loads from the
63 Changjiang (Liu et al., 2015).

64 It is generally accepted that water-column stratification and the decomposition of
65 organic matter are the two essential factors for hypoxia generation, and this is also the case
66 for the shelf region off the CE (Chen et al., 2007; Li et al., 2002; Wei et al., 2007). High
67 solar radiation and FW input in summer contribute to strong vertical stratification which is
68 further enhanced by near-bottom advection of waters with high salinities (> 34) and low
69 temperatures (< 19 °C) by the Taiwan Warm Current. The resulting strong stratification
70 inhibits vertical oxygen supply (Li et al., 2002; Wang, 2009; Wei et al., 2007). At the same
71 time, high organic matter supply fuels microbial oxygen consumption in the subsurface (Li
72 et al., 2002; Wang, 2009; Wei et al., 2007; Zhu et al., 2011). It has also been suggested that
73 the Taiwan Warm Current brings additional nutrients contributing to organic matter
74 production (Ning et al., 2011) and that the low oxygen concentrations (~ 5 mg L⁻¹) of the
75 Taiwan Warm Current precondition the region to hypoxia (Ning et al., 2011; Wang, 2009).

76 While observational analyses suggest that hypoxia off the CE results from the interaction
77 of various physical and biogeochemical processes, quantifying the relative importance of
78 these processes and revealing the dynamic mechanisms underlying hypoxia development
79 and variability require numerical modeling (Peña et al., 2010). Numerical modeling studies
80 have proven useful for many other coastal hypoxic regions such as the Black Sea
81 northwestern shelf (Capet et al., 2013), Chesapeake Bay (Li et al., 2016; Scully, 2013), and
82 the northern Gulf of Mexico (Fennel et al., 2013; Laurent & Fennel, 2014).

83 Models have also been used to study the hypoxic region of the CE. Chen et al. (2015a)
84 used a 3D circulation model with a highly simplified oxygen consumption parameterization
85 (a constant consumption rate) to investigate the effects of physical processes, i.e. FW
86 discharge, and wind speed and direction, on the dissipation of hypoxia. Chen et al. (2015b)
87 examined the tidal modulation of hypoxia. The model domain in these two previous studies
88 was relatively limited encompassing only the CE, Hangzhou Bay and the adjacent coastal
89 ocean but did not cover the whole area affected by hypoxia (Wang, 2009; Zhu et al., 2011).
90 Zheng et al. (2016) employed a nitrogen cycle model coupled with a 3D hydrodynamic
91 model to examine the role of river discharge, wind speed and direction on hypoxia, and

92 also emphasized the physical controls. These previous modeling studies focused on the
93 response of hypoxia to physical factors only and did not address seasonal evolution and
94 interannual variations of hypoxia or the influence of variability in biological rates.

95 More recently, Zhou et al. (2017) analyzed the seasonal evolution of hypoxia and the
96 importance of the Taiwan Warm Current and Kuroshio intrusions as a nutrient source using
97 an advanced coupled hydrodynamic-biological model. However, the baseline of their
98 model does not include sediment oxygen consumption (SOC), which is thought to be a
99 major oxygen sink in the hypoxic region off the CE (Zhang et al., 2017) and other river-
100 dominated hypoxic regions including the northern Gulf of Mexico (Fennel et al. 2013, Yu
101 et al. 2015a,b). Zhou et al. (2017) acknowledged the importance of SOC based on results
102 from a sensitivity experiment but did not quantify its role in hypoxia generation.

103 Here we introduce a new 3D physical-biological model implementation for the ECS that
104 explicitly includes nitrogen and phosphorus cycling and SOC. The model is a new regional
105 implementation for the ECS of an existing physical-biogeochemical model framework that
106 has been extensively used and validated for the northern Gulf of Mexico (Fennel et al.,
107 2011, 2013; Laurent et al., 2012; Laurent and Fennel, 2014; Yu et al., 2015b; Fennel and
108 Laurent, 2018). The hypoxic zones in the northern Gulf of Mexico and off the CE have
109 similar features including the dominant influence of a major river (Changjiang and
110 Mississippi), a seasonal recurrence every summer, a typical maximum size of about 15,000
111 km², documented P-limitation following the major annual discharge in spring and a
112 significant contribution of SOC to oxygen sinks in the hypoxic zone (Fennel and Testa
113 2019).

114 We performed and assessed a 6-year simulation of the ECS, and use the model results
115 here to identify the main factors driving hypoxia variability on interannual and intra-
116 seasonal timescales in the simulation. More specifically, we investigate the role of
117 interannual variations in riverine inputs of nutrients and FW versus intra-seasonal
118 variations in coastal circulation and mixing. We also present an oxygen budget to quantify
119 the relative importance of SOC and the influence of lateral advection of oxygen. A
120 companion study by Grosse et al. (2020) uses the same model to quantify the importance
121 of intrusions of nutrient-rich oceanic water from the Kuroshio for hypoxia development off
122 the CE.

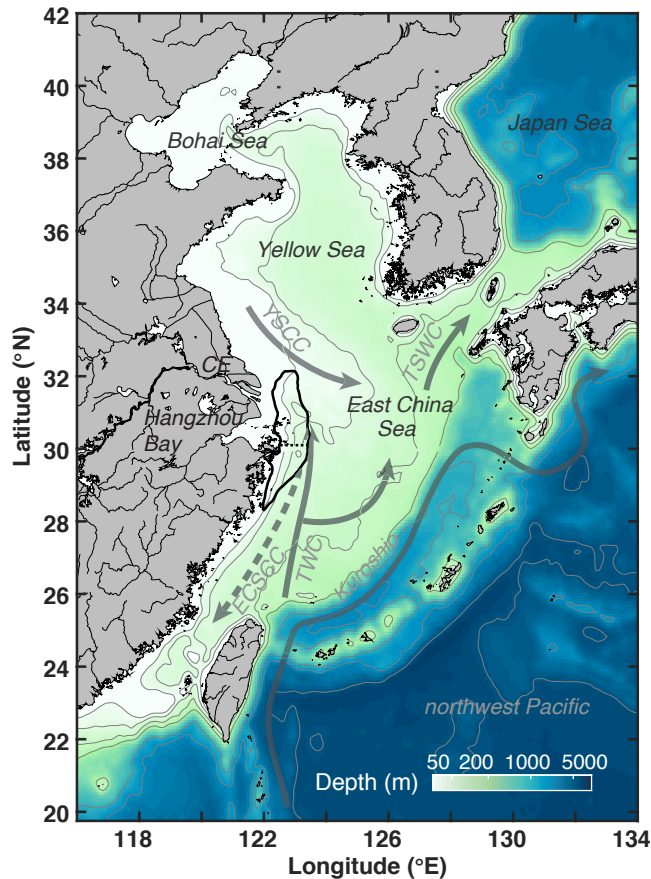
123 **2. Model description**

124 **2.1. Physical model**

125 The physical model used in this study is based on the Regional Ocean Modeling System
126 (ROMS; Haidvogel et al., 2008) and was implemented for the ECS by Bian et al. (2013a).
127 The model domain extends from 116°E to 134°E and from 20°N to 42°N (Figure 1),
128 covering the Bohai Sea, the Yellow Sea, the ECS, part of the Japan Sea and the adjacent
129 northwest Pacific, with a horizontal resolution of 1/12° (about 10 km) and 30 vertical layers
130 with enhanced resolution near the surface and bottom. The model uses the recursive
131 Multidimensional Positive Definite Advection Transport Algorithm (MPDATA) for the
132 advection of tracers (Smolarkiewicz and Margolin, 1998), a third-order upstream advection
133 of momentum, and the Generic Length Scale (GLS) turbulence closure scheme (Umlauf &
134 Burchard, 2003) for vertical mixing.

135 The model is initialized with climatological temperature and salinity from the World
136 Ocean Atlas 2013 V2 (WOA13 V2) (Locarnini et al., 2013; Zweng et al., 2013), and is
137 forced by 6-hourly wind stress, and heat and FW fluxes from the ECMWF ERA-Interim
138 dataset (Dee et al., 2011). Open boundary conditions for temperature and salinity are
139 prescribed from the monthly climatology (WOA13 V2), and horizontal velocities and sea
140 surface elevation at the boundaries are specified from the monthly SODA data set (Carton
141 & Giese, 2008). In addition, eight tidal constituents (M2, S2, N2, K2, K1, O1, P1 and Q1)
142 are imposed based on tidal elevations and currents extracted from the global inverse tide
143 model data set of TPXO7.2 of Oregon State University (OSU, Egbert & Erofeeva, 2002).
144 At the open boundaries, Chapman and Flather conditions are used for the free surface and
145 the barotropic velocity, respectively, and the radiation condition for the baroclinic velocity.
146 Eleven rivers are included in the model. FW discharge from the Changjiang uses daily
147 observations from the Datong Hydrological Station (DHS; www.cjh.com.cn). Since daily
148 observations are not available for the other rivers, we prescribed monthly or annual
149 climatologies (Liu et al., 2009; Tong et al., 2015; Zhang, 1996).

150



151

152 **Figure 1.** Bathymetry of the model domain with 30, 50, 100, 200, 1000, 2000 and 5000 m isobaths.
 153 The black outline near the Changjiang Estuary (CE) and Hangzhou Bay indicates the zone typically
 154 affected by low-oxygen conditions (dotted line shows separation between northern and southern
 155 zones). Solid grey arrows denote currents present throughout the year (Kuroshio; TWC: Taiwan
 156 Warm Current; YSCC: Yellow Sea Coastal Current). The dashed grey arrow indicates the direction
 157 of the wintertime East China Sea Coastal Current (ECSCC) which flows in the opposite direction
 158 to summertime flow.

159

160 **2.2. Biological model**

161 The biological component is based on the pelagic nitrogen cycle model of Fennel et al.
 162 (2006, 2011, 2013) and was extended to include phosphate (Laurent et al., 2012; Laurent
 163 & Fennel, 2014) and riverine dissolved organic matter (Yu et al., 2015b). The model
 164 includes two forms of dissolved inorganic nitrogen (DIN), nitrate (NO₃) and ammonium
 165 (NH₄), phosphate (PO₄), phytoplankton (Phy), chlorophyll (Chl), zooplankton (Zoo), two
 166 pools of detritus, suspended and slow-sinking small detritus (SDet) and fast-sinking large

167 detritus (LDet), and riverine dissolved organic matter (RDOM). Here, riverine dissolved
168 and particulate organic nitrogen enter the pools of RDOM and SDet, respectively. The
169 remineralization rate of RDOM is an order of magnitude lower than that of SDet to account
170 for the more refractory nature of the riverine dissolved organic matter (Yu et al., 2015b).

171 At the sediment-water interface, SOC is parameterized assuming “instantaneous
172 remineralization,” i.e. all organic matter reaching the sediment is remineralized
173 instantaneously and oxygen is consumed due to nitrification and aerobic remineralization
174 at the same time. In the “instantaneous remineralization”, all phosphorus is returned to the
175 water column as PO₄ while a constant fraction of fixed nitrogen is lost due to denitrification.
176 All biogeochemical model parameters are given in Table S1 in the Supplement. A more
177 detailed model descriptions can be found in the Supplement to Laurent et al. (2017).

178 Light is vertically attenuated by chlorophyll, detritus and seawater itself. In addition, to
179 account for the effects of colored dissolved organic matter (CDOM) and suspended
180 sediments, which show relatively high values near the coast and in the river plume (Bian
181 et al., 2013b; Chen et al., 2014), a light-attenuation term dependent on water depth and
182 salinity is introduced which yields higher attenuation in shallow areas and in the FW plume.

183 Initial and boundary conditions for NO₃, PO₄ and oxygen are prescribed using the
184 World Ocean Atlas 2013 (WOA13) climatology (Garcia et al., 2013a,b). A small positive
185 value is used for the other variables. NO₃ is nudged towards climatology in the northwest
186 Pacific at depth > 200 m. Monthly nutrient loads of NO₃ and PO₄ from the Changjiang are
187 from the Global-NEWs Model (Wang et al., 2015) but were adjusted by multiplicative
188 factors of 1.20 and 1.66, respectively, to ensure a match between simulated and observed
189 nutrient concentrations in the CE (see July and Aug 2012 in Figure 2). Nutrient loads in
190 other rivers are based other published climatologies (Liu et al., 2009; Tong et al., 2015;
191 Zhang, 1996). Due to a lack of data on organic matter loads, river load concentrations of
192 SDet and LDet and RDOM were assumed conservatively at 0.5, 0.2 and 15 mmol N m⁻³,
193 respectively.

194 We performed an 8-year simulation from 1 January 2006 to 31 December 2013, with
195 2006-2007 as model spin up and 2008-2013 used for analysis. Model output was saved
196 daily.

197

198 **3. Results**

199 **3.1. Model validation**

200 Model output is compared with observations of simulated surface and bottom
201 temperature, salinity, current patterns and strength, surface chlorophyll, surface nitrate and
202 bottom oxygen. The model reproduces remotely sensed spatial and temporal SST patterns
203 (NOAA AVHRR) very well (Figure S1) with an overall correlation coefficient, i.e.
204 considering all climatological monthly mean SST fields interpolated to the model grid, of
205 0.98. Simulated surface and bottom salinity also show similar spatial and seasonal patterns
206 as available *in situ* observations (Figures S2 and S3) with overall correlation coefficients,
207 i.e. using all surface and all bottom data points, of 0.77 and 0.84, respectively. Simulated
208 surface and bottom temperature, when compared with available *in situ* data (Figures S4
209 and S5), are also consistent with the observations with overall correlation coefficients of
210 0.96 and 0.93.

211 The simulated current systems in the ECS and YS show typical seasonal variations as
212 follows (see also Figure S6). In winter, currents mainly flow southward on the Yellow Sea
213 and ECS shelves driven by the northerly wind. In contrast, the East China Sea Coastal
214 Current and the Korean Coastal Current flow northward in summer. The Kuroshio is

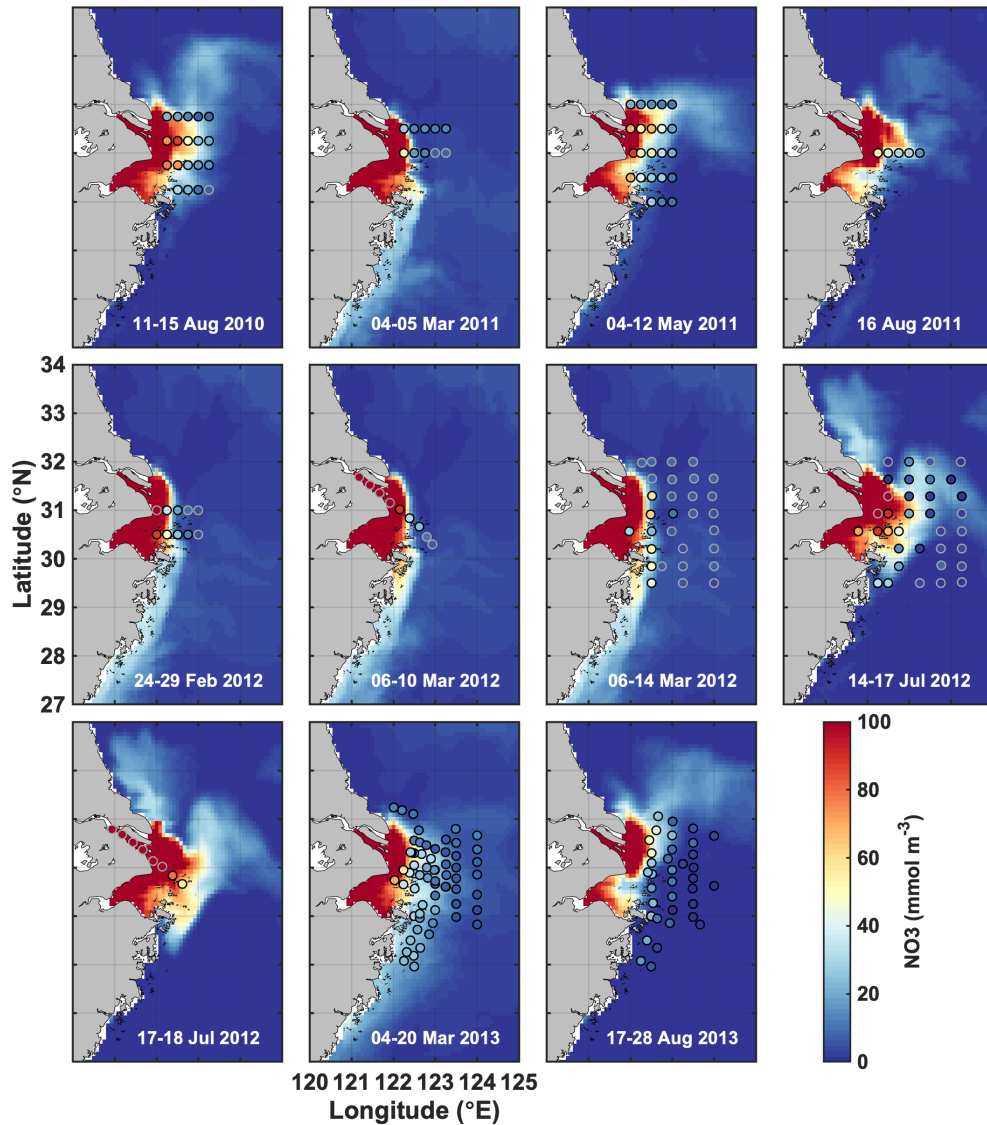


Figure 2: Simulated surface nitrate (colored map) shown for the day that marks the mid-point of the cruise dates (given in each panel) the compared to observations (dots) during 11 cruises from 2011 to 2013.

215 stronger in summer than in winter. The model captures the seasonal pattern of the current
 216 system and resolves currents in the ECS and Yellow Sea (also see Grosse et al. 2020).

217 Simulated monthly averaged (2008-2013) surface chlorophyll concentrations in May,
 218 August and November are compared with satellite-derived fields (MODIS-Terra) and
 219 agree well with spatial correlation coefficients of 0.77, 0.94 and 0.64, respectively (Figure
 220 S7).

221 Simulated surface nitrate concentrations are shown in comparison to *in situ* observations
 222 in Figure 2 and agree well with an overall correlation coefficient of 0.84. Observations in
 223 March and July of 2012 show strongly elevated concentrations in the CE and a sharp
 224 gradient in the vicinity of the estuary's mouth that are well represented by the model.
 225 Likewise, simulated and observed bottom oxygen distributions are compared in Figure 3
 226 and agree reasonably well overall with an overall correlation coefficient of 0.71 although
 227 the model underestimates observed low-oxygen conditions in July of 2011 and 2013 and
 228 August 2013.

229 Together, these comparisons show that the model is able to reproduce important aspects
 230 of the physical-biogeochemical dynamics in the study region.

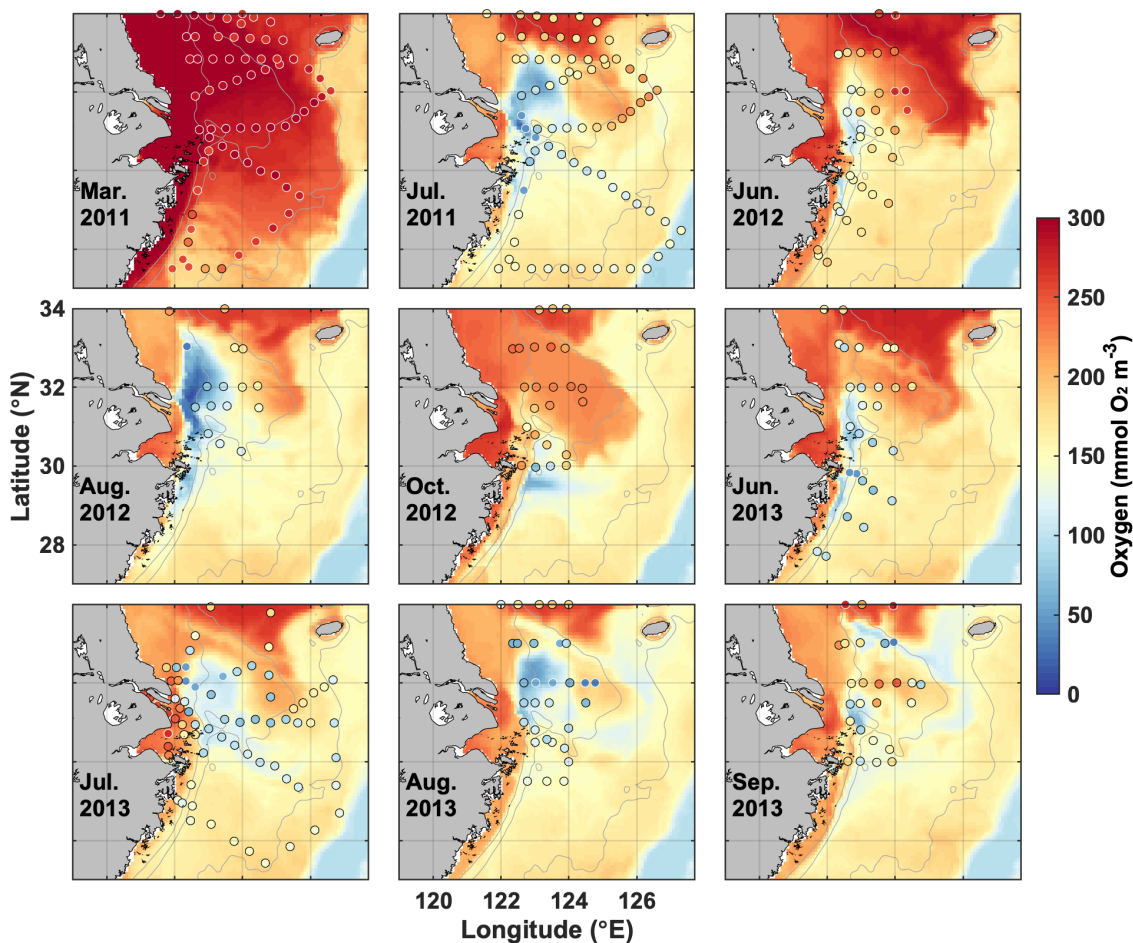


Figure 3. Simulated bottom oxygen (colored map) shown for the day that marks the mid-point of the cruise dates compared with observations (dots) during nine cruises from 2011 to 2013.

232 **3.2. Simulated oxygen dynamics**

233 First, we describe the timing and distribution of simulated bottom-water oxygen off the
 234 CE to set the stage for our investigation into the drivers underlying hypoxia variability. The
 235 model simulates annually recurring hypoxic conditions with a typical seasonal cycle where
 236 bottom waters are well-oxygenated until April/May, hypoxic conditions establish in June
 237 or July, become more pronounced in August, and disperse in October or November (Figure
 238 4a, c). However, the model also simulates significant interannual variability in timing and
 239 extent of hypoxia over the 6-year simulation period (Figure 4b, c). The years with largest
 240 maximum hypoxic extent are 2010 (20,520 km²), 2009 (16,660 km²), 2012 (13,930 km²)
 241 and 2008 (12,720 km²) while the simulated hypoxic extent is much smaller (<5,000 km²)
 242 in 2011 and 2013. The ranking is similar when considering the time-integrated hypoxic
 243 extent (Figure 4b). The year with the largest maximum and integrated hypoxic extent

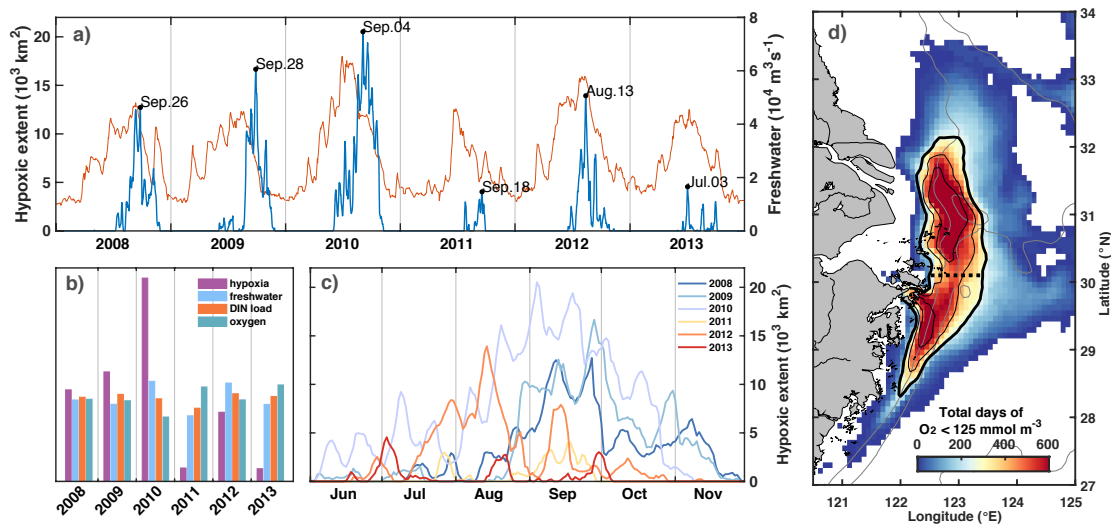


Figure 4. a) Time series of freshwater discharge (thin red line) and simulated hypoxic extent (thick blue line) with peaks specified by date. b) Annual comparison of normalized time-integrated hypoxic extent, freshwater discharge, and DIN load, and summer-mean bottom oxygen concentration. c) Evolution of simulated hypoxic extent by year. d) Frequency map of number of days when bottom oxygen concentrations were below 125 mmol m⁻³ (4 mg/l). The black isolines indicate 240, 360 and 480 days (or 40, 60 and 80 days per year). The thick solid line indicates the region we refer to as the typical low-oxygen zone and the dashed line shows the demarcation between its northern and southern regions.

244 (2010) also has the highest peak discharge (Figure 4a) and highest annual FW discharge
245 ($65,400 \text{ m}^3 \text{ s}^{-1}$), although the annual discharge in 2008 and 2012 is not much smaller than
246 in 2010.

247 The region where low-oxygen conditions are most commonly simulated is indicated by
248 the frequency map in Figure 4d, which shows the total number of days in the 6-year
249 simulation when bottom oxygen concentrations were below 125 mmol m^{-3} (or 4 mg/l), i.e.
250 twice the hypoxic threshold. It is known from observations that there are two centers of
251 recurring hypoxic conditions: the northern core is located just to the east of the CE and
252 Hangzhou Bay and the southern core to the southeast of Hangzhou Bay. The model is
253 consistent with these observations and simulates two distinct core regions of low-oxygen
254 conditions centered at 31°N and 29.3°N . The northern core region is larger than the
255 southern core region ($9,050 \text{ km}^2$ for a threshold of 80 days per year of $< 4 \text{ mg/l}$ compared
256 to $5,230 \text{ km}^2$). We will refer to the region defined by a threshold of 40 days of $< 4 \text{ mg/l}$
257 per year (solid black line in Figure 1 and 4d) as the “typical low-oxygen zone” for the
258 remainder of the manuscript and demarcate the northern and southern sections by 30.1°N
259 latitude (dashed line in Figures 1 and 4d).

260 There are marked differences in the phenology of simulated hypoxic extent (Figure 4c).
261 Among the four years with largest hypoxic areas, hypoxia establishes relatively late (mid-
262 August) and lasts long (into November) in 2008 and 2009. In contrast in 2012, hypoxic
263 conditions establish earlier (June), are most pronounced in August and are eroded by mid-
264 October. In 2010, the year with the largest peak extent, hypoxia establishes already at the
265 beginning of June and is maintained until the end of October, leading to the largest time-
266 integrated hypoxia by far among the 6 years (Figure 4b). In all years there are times when
267 hypoxic extent decreases rapidly.

268 In the following sections, we explore the drivers underlying these interannual and intra-
269 seasonal variations, specifically the contribution of year-to-year variations in nutrient loads
270 and FW inputs from the Changjiang, and the potential reasons for intra-seasonal variability
271 in hypoxia by assessing the role of biological processes and physical forcing.

272
273
274

275 3.2.1 Interannual variations in hypoxia

276 The first question we address is: Do year-to-year variations in nutrient load and FW input
 277 from the Changjiang explain interannual variability in hypoxic conditions? We do this by
 278 investigating correlations of time-integrated hypoxic area, average PP, total oxygen
 279 consumption (OC) by respiration, SOC, and bottom oxygen in the typical low-oxygen zone
 280 (Figure 5 a-f). We also consider the correlation between the spatial extent of the FW plume,
 281 defined as the horizontal extent of surface water with salinity less than 29, and annually
 282 integrated FW input and DIN load (Figure 5 g-i).

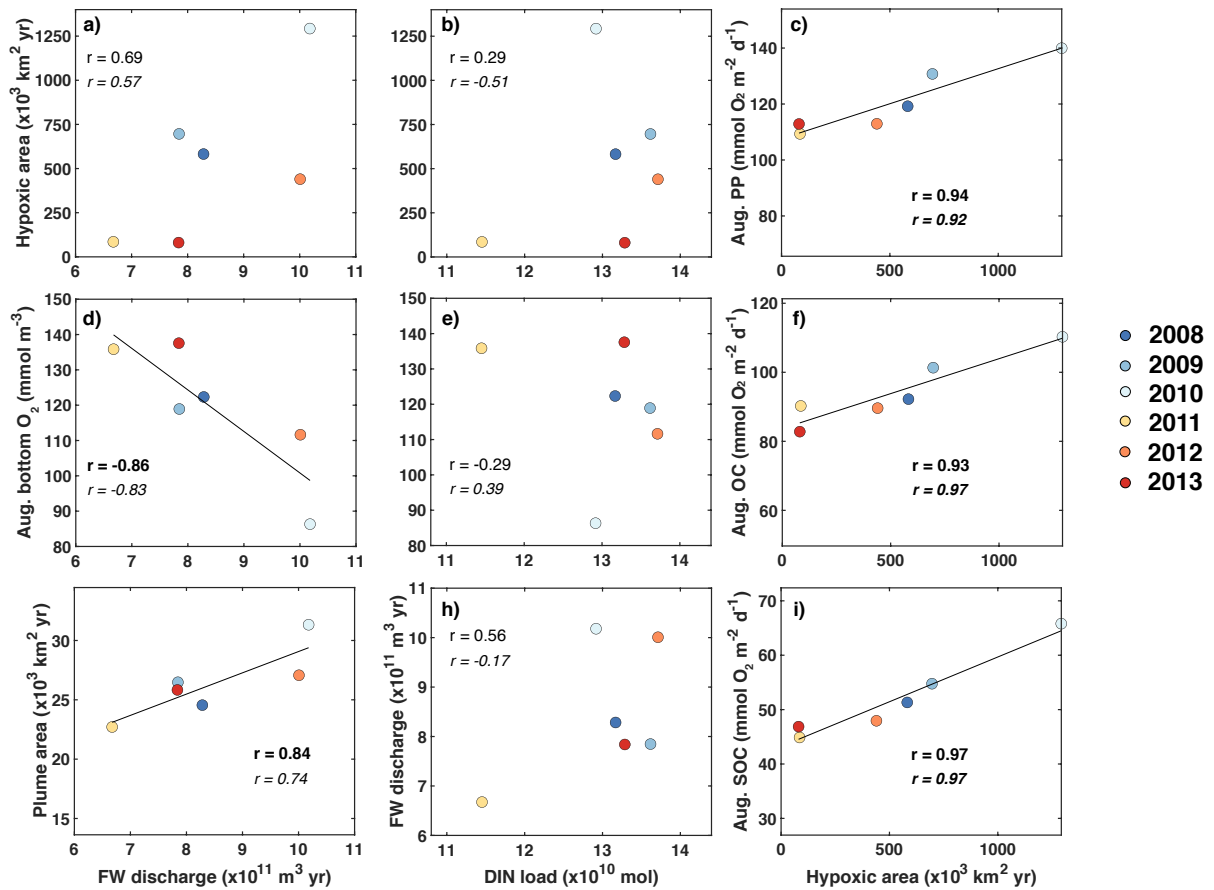


Figure 5. Correlations of time-integrated hypoxic area, average primary production, respiration and bottom oxygen in the typical low-oxygen zone in August, and the spatial extent of the FW plume (defined here as the area with surface salinity smaller than 29) with annually integrated FW input and DIN load. Correlation coefficients are given for all 6 years and, in italic font, after excluding year 2011. Significant correlations are shown in bold font and linear regressions indicated by the black line whenever the correlation is significant at $p < 0.05$.

283 There is a significant negative correlation between annual FW input and mean bottom-
284 water oxygen concentration in the low-oxygen zone of -86% and a weaker, statistically
285 insignificant positive correlation of 69% between annual FW input and integrated hypoxic
286 area (Figure 5a, d). This indicates that variations in FW input at least partly explain
287 variability in hypoxic conditions. Perhaps surprisingly, there is no convincing correlation
288 between annual FW input and annual DIN load (Figure 5h). Although the correlation
289 coefficient is 56% when all 6 years are considered, the correlation reverses to -17% when
290 the low-flow year 2011 is excluded and neither of these correlations is statistically
291 significant. As expected, there is a strong positive correlation of 84% between the annual
292 FW input and time-integrated plume area (Figure 5g). Plume area can thus be interpreted
293 as a proxy of FW input.

294 In contrast to the positive correlations between FW input and hypoxia, and FW input
295 and bottom oxygen, correlations between the annual DIN load with integrated hypoxic area
296 and mean bottom-water oxygen are much weaker and insignificant (Figure 5b, e). This
297 implies that interannual variations in DIN load do not lead to year-to-year variations in
298 hypoxia. However, the correlations between integrated hypoxic area and mean rates of PP
299 and OC (especially SOC) in August are significant and strong at 94% and 93% (97%),
300 respectively (Figure 5c, f, i). The high correlation between hypoxic area and OC is
301 primarily driven by SOC. Clearly, biological processes are important drivers of hypoxia
302 and contribute to its interannual variability, but they do not appear to result from variations
303 in DIN load. More relevant are variations in FW load, which explain interannual variations
304 in hypoxia at least partly.

305 Clearly, other factors than riverine inputs of nutrients and FW must be contributing to
306 interannual variations. For example, the years 2010 and 2012 both had very similar FW
307 input and DIN load but differed in severity of hypoxia (Figure 5a, b). Likewise, the years
308 2009 and 2013 were very similar in terms of FW input and DIN load, but very different in
309 hypoxic extent. Next, we investigate the potential reasons for intra-seasonal variability in
310 hypoxia, i.e. the processes leading to the differences in hypoxia phenology in Figure 4c.

311

312

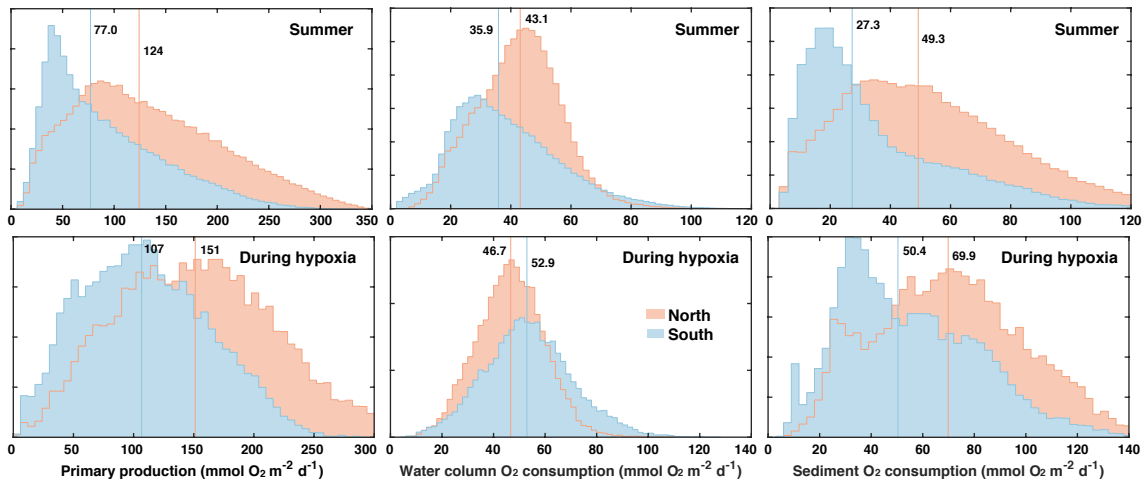
313

314 *3.2.2 Biological drivers of intra-seasonal variability in hypoxia*

315 In the previous subsection, we identified biological rates as important drivers of low-
316 oxygen conditions on interannual timescales but unrelated to variations in riverine DIN
317 load. Here we attempt to elucidate what drives variations in biological rates and low-
318 oxygen conditions on intra-seasonal scales by addressing the following two questions. Do
319 low-oxygen conditions correlate with biological rates on these shorter timescales? If yes,
320 what drives variations in biological rates?

321 For this analysis it seems prudent to distinguish between the northern and southern
322 hypoxic regions for the following reasons. The bathymetry in the northern zone is slightly
323 deeper than in the southern zone (median depth of 28.5 m versus 24.6 m) and several
324 biological rates with direct relevance to oxygen dynamics are different between the two
325 zones (Figure 6). During the summer months (June to September), PP, oxygen
326 consumption in the water column (WOC=OC-SOC), and SOC are larger in the northern
327 zone with medians of 124 compared to 77.0 mmol O₂ m⁻² d⁻¹ for PP, of 43.1 versus 35.9
328 mmol O₂ m⁻² d⁻¹ for WOC, and 49.3 versus 27.3 mmol O₂ m⁻² d⁻¹ for SOC. During hypoxic
329 conditions, PP and SOC are also notably larger in the northern zone with medians of 151
330 versus 107 mmol O₂ m⁻² d⁻¹ for PP and 69.9 versus 50.4 mmol O₂ m⁻² d⁻¹ for SOC. In the
331 water column, the difference is reversed and WOC larger in the southern than the northern
332 zone (52.9 versus 46.7 mmol O₂ m⁻² d⁻¹). Because of these different characteristics, we
333 consider the northern and southern zones of the typical low-oxygen region separately.

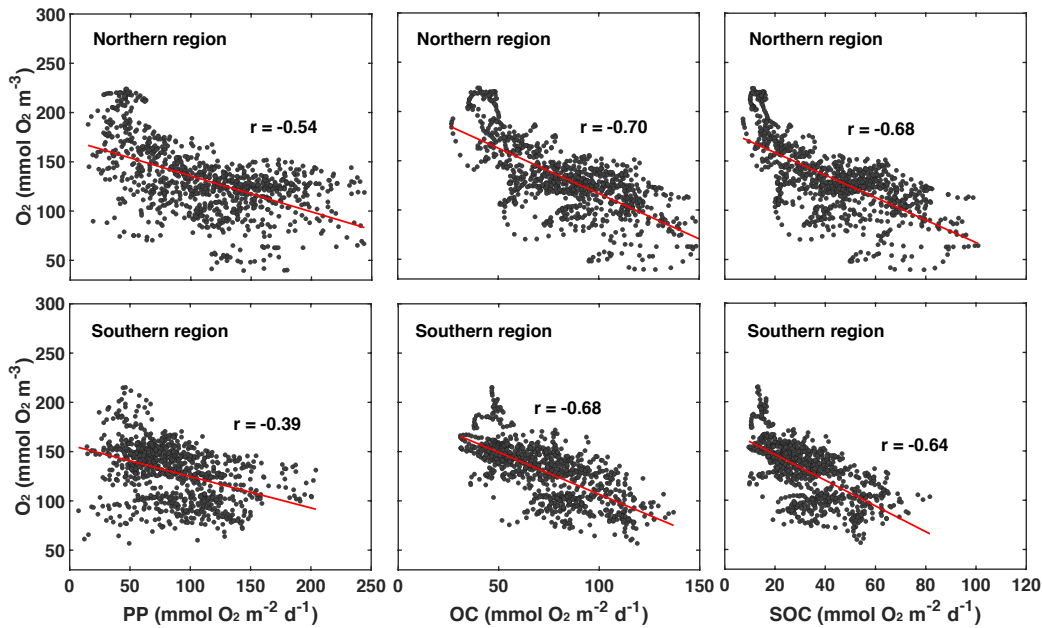
334 First, we explore whether significant relationships exist between daily biological rates
335 and bottom-water oxygen by determining the correlations of daily averaged rates of PP,
336 OC and SOC with daily mean bottom oxygen concentration (Figure 7 and Table 1).



337

338 **Figure 6:** Histograms primary production and water-column and sediment respiration during the
 339 summer months (June to September) and during hypoxic conditions in the northern and southern
 340 parts of the typically hypoxic zone. Medians are indicated by vertical lines.

341



342

343 **Figure 7.** Correlations of daily averaged rates of PP, OC and SOC plotted with daily mean
 344 bottom oxygen concentration in the northern and southern regions of the low-oxygen zone in
 345 summer. The correlations are all significant. Correlation coefficients and slope and intercept of
 346 linear regressions (indicated by red lines) are given in Table 1.

347

348

Relationships between bottom oxygen (mmol m ⁻³) in northern region and											
PP (mmol O ₂ m ⁻² d ⁻¹)			OC (mmol O ₂ m ⁻² d ⁻¹)			SOC (mmol O ₂ m ⁻² d ⁻¹)					
r	a	b	r	a	b	r	a	b			
-0.54	-0.36	172	-0.70	-0.92	209	-0.68	-1.14	181			
Same for the southern region											
-0.39	-0.32	157	-0.68	-0.85	192	-0.64	-1.30	172			
Relationships between plume area (10 ³ km ² ; defined by surface salinity < 29) in northern region											
PP (mmol O ₂ m ⁻² d ⁻¹)			OC (mmol O ₂ m ⁻² d ⁻¹)			SOC (mmol O ₂ m ⁻² d ⁻¹)			Bottom oxygen (mmol m ⁻³)		
0.62	6.04	47.6	0.49	2.48	57.7	0.51	2.05	22.0	-0.56	-3.74	171
Same for the southern region											
0.43	3.78	64.6	0.56	3.18	57.8	0.43	1.50	24.7	-0.49	-3.52	149

349 **Table 1.** Correlation coefficients and parameters of a linear model fit (of the form $y=ax+b$) between

350

351 Indeed, daily PP, OC, and SOC are all significantly and negatively correlated with
352 bottom-water oxygen. This confirms that local production of organic matter and the
353 resulting biological oxygen consumption are important for hypoxia development and that
354 variations in these rates partly explain variations in low-oxygen conditions. However, it is
355 also obvious that variability around the best fit is large (Figure 7).

356 The next question is: What drives variations in the biological rates? Since the annual
357 correlations presented in the previous section indicate that variability in annual FW input
358 partly explains interannual variability in hypoxia, we consider whether FW variability is
359 related to variations in biological rates. Using daily plume extent as a measure of FW
360 presence and comparing it to daily rates of PP, OC, SOC, and bottom oxygen, we find that
361 bottom oxygen and biological rates are significantly correlated with the extent of the FW
362 plume with correlation coefficients ranging from 43% to 62% (Table 1). In other words,
363 variability in the extent of the FW plume explains roughly half of the variability in
364 biological rates. Mechanistically, the presence of a large FW plume not only affects
365 hypoxia by increasing vertical stratification and thus inhibiting vertical supply of oxygen
366 to the subsurface but also because PP and respiration is larger in the plume. Large FW
367 plumes stimulate more widespread biological production and thus oxygen consumption.

368 Since annual FW input is highly correlated with the extent of the FW plume (see Figure
369 5g), variability in its extent is partly due to variations in riverine input, but coastal
370 circulation and mixing processes must be playing a role as well. Next, we analyze the
371 impact of the underlying physical drivers.

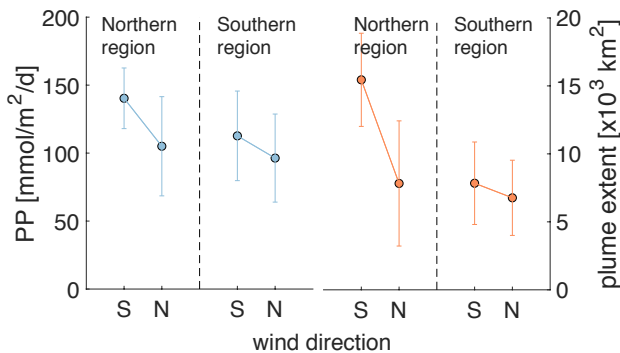
372

373 3.2.3 Physical drivers of intra-seasonal variability in hypoxia

374 We focus our analysis of physical drivers on wind direction and wind strength, and their
375 relation to FW plume location and extent because the latter has already been identified as
376 an explanatory variable for interannual variations in the previous section.

377 Wind direction is relevant because for most of June, July, and August winds blow
378 predominantly from the south, but switch to predominantly northerly winds between the
379 second half of August and the end of September. As a result of the northward, upwelling
380 favorable winds in the early summer, the FW plume is spread offshore and overlaps
381 primarily with the northern zone. After the switch to mostly southward, downwelling-
382 favorable directions, the FW plume moves southward, becomes more contained near the
383 coast, and grows in its southward extent as it is transported by a coastal current. Wind
384 direction has a demonstrable impact on PP and the extent of the FW plume as shown in
385 Figure 8 for the month of September. Especially in the northern region, PP and plume
386 extent are notably larger during southerly winds when the FW plume is more spread out,
387 than during northerly winds when the plume is more restricted within the coastal current.

388



389

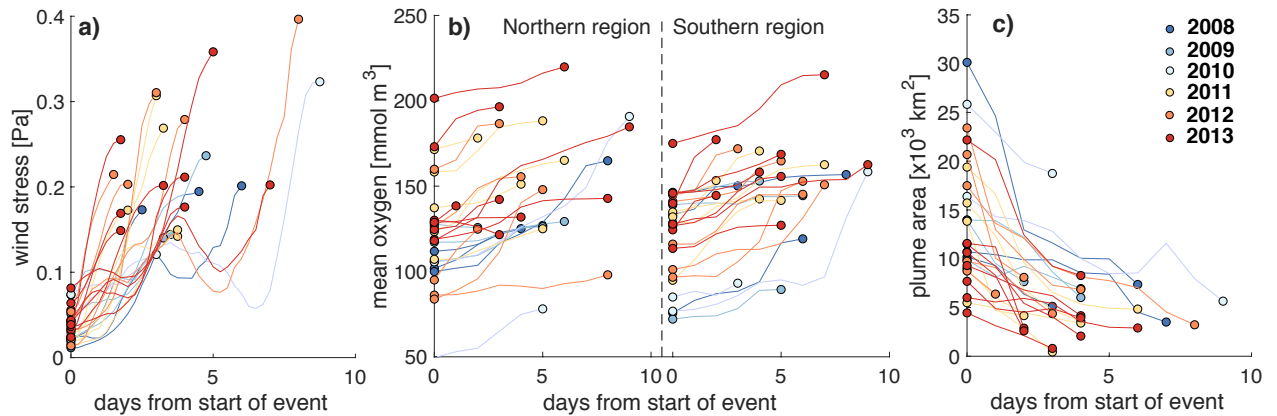
390 **Figure 8.** Mean PP and FW plume extent in the northern and southern regions averaged over all
391 days during the 6-yr simulation with north and south wind (i.e. when direction is +/- 45° of true
392 north or south) and wind strength >0.03 Pa for in September.

393

394 Wind strength is relevant because storm events can erode vertical stratification and thus
395 lead to resupply of oxygen to bottom waters due to vertical mixing. We investigated the
396 effect of wind strength on bottom oxygen, hypoxia, and the extent of the FW plume by first
397 inspecting time series of these variables (Figure S8). We isolated all event during the

398 months June to September and, in Figure 10, show the corresponding changes in wind
399 stress, mean bottom oxygen in the northern and southern zones, and the extent of the FW
400 plume. We diagnosed these events as follows. First, we identified all days when the wind
401 stress exceeded 0.12 Pa. Then we detected the minima in wind stress adjacent to the high-
402 wind days by searching for minima in wind stress within 3 days prior and 3 days after the
403 high-wind days. The periods within these minima are used as analysis period for each wind
404 event. In four instances the wind stress exceeded the threshold within 5 days of a previous
405 wind event. Those subsequent high-wind events were combined into one. We identified
406 the minimum in bottom oxygen (maximum in FW plume area) at the beginning of the event
407 and the maximum in oxygen (minimum in FW area) after the maximum in wind stress was
408 reached.

409 Figure 9a illustrates rapid increases in wind stress typically within 2 to 4 days. The only
410 exceptions are the 4 events where two storms occurred in rapid succession and the
411 combined event lasted longer (up to 8 days) until maximum wind stress was reached. The
412 year with the most wind events is 2013 (with 8 in total including one of the combined long-
413 lasting event). The year with the least events is 2010 (2 events) followed by 2009 (3 events).
414 Most of these events resulted in notable increases in mean bottom oxygen, typically by 10
415 to 30 mmol m⁻³, but up to 100 mmol m⁻³ in 2010 in the southern zone (Figure 9b). In the
416 rare cases where bottom oxygen did not increase or slightly decreased, bottom oxygen was
417 already elevated before the wind event. The wind events strongly affected the extent of the
418 FW plume (Figure 9c) by mixing the FW layer with underlying ocean water. The effects
419 were largest when the FW plume was most expansive. This analysis shows the significant
420 role of storm events in disrupting the generation of low-oxygen conditions and ventilating
421 bottom waters.

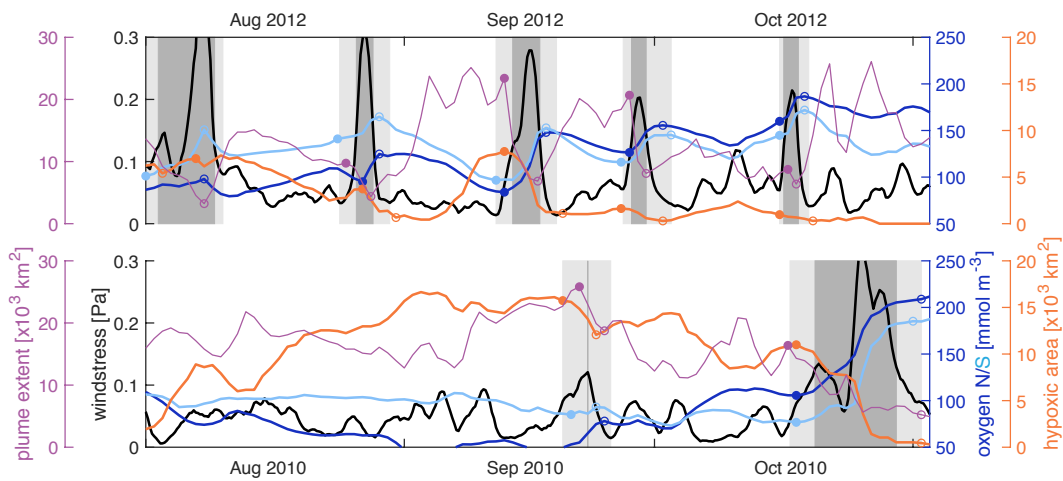


422

423 **Figure 9.** Evolution of a) wind stress, b) bottom mean oxygen in the northern and southern regions,
 424 and c) extent of the FW plume during high-wind events. These events are defined by wind stress
 425 exceeding 0.12 Pa.

426

427 In section 3.2.1 above, we noted that while the years 2010 and 2012 had very similar
 428 FW input and DIN load, 2010 had a much larger hypoxic area. Likewise, the years 2009
 429 and 2013 were very similar in terms of FW input and DIN load, but 2009 had a much larger
 430 hypoxic area. It now becomes obvious that the frequency and severity of high-wind events
 431 explains the differences in both cases.



432

433 **Figure 10.** Wind stress (black), mean bottom oxygen in the northern and southern zones (dark and
 434 light blue), total hypoxic extent (orange), and FW plume extent (purple) throughout August,
 435 September and October of 2010 and 2012. The filled and open circles indicate a variables' value at

436 the beginning and after high-wind events. High-wind days/events are indicated by the dark/light
437 gray shading.

438 Figure 10 shows the wind stress, mean bottom oxygen in the northern and southern
439 zones, and total hypoxic extent and FW plume extent in 2012 and 2010. In 2012, there
440 were 5 high-wind events during the months of August, September, and October that all
441 coincided with increases in bottom oxygen, decreases in hypoxic extent when a hypoxic
442 zone was established at the beginning of the event, and decreases in FW plume extent.
443 Inspection of the evolution of bottom oxygen is especially instructive. While bottom
444 oxygen concentrations declined during periods with average or low wind, they were
445 essentially reset at a much higher level during each wind event. Whenever the FW plume
446 was extensive at the beginning of a high-wind event, it was drastically reduced during the
447 event. In 2010, bottom oxygen was at similar levels to 2012 at the beginning of August but
448 dropped to low levels throughout August, especially in the northern zone, and remained
449 low with widespread hypoxia until a major wind event in the second half of October
450 ventilated bottom waters. Except for a very short event in the second half of September,
451 there were no high-wind events from August until mid-October in 2010.

452 The differences in hypoxia in 2009 and 2013 can also be explained by the frequency and
453 intensity of high-wind events. In 2013, there were 8 high-wind events from July to October
454 that led to an almost continuous ventilation of bottom waters while in 2009 there were only
455 3 such events during the same period (Figure S8). Low to average winds from mid-August
456 to early October of 2009 coincided with a decline in bottom oxygen and establishment of
457 an expansive hypoxic zone throughout most of September.

458 These analyses show that wind direction and strength play an important role in
459 determining the location of the hypoxic zone (i.e. northern versus southern region) and the
460 extent and severity of hypoxic conditions.

461

462 ***3.3 Oxygen budgets for the northern and southern regions***

463 In order to further investigate the roles of physical and biological processes in regulating
464 hypoxia, oxygen budgets were calculated from daily model output for the period from
465 March to November for the northern and southern hypoxic regions. Considering that
466 hypoxic conditions occur near the bottom, we evaluate an oxygen budget not only for the

467 whole water column but also for its lower portion which typically becomes hypoxic. To
468 account for variations in the thickness of the hypoxic layer, which tends to be thicker in
469 deeper waters (similar to observations by Ning et al., 2011), we include the bottommost 12
470 layers of our model grid. Because of the model's terrain-following vertical coordinates, the
471 thickness of these 12 model layers varies with total depth. The terms considered in the
472 budget are air-sea flux, lateral physical advection and diffusion, vertical turbulent diffusion
473 (for the subsurface budget only), PP, WOC (including respiration and nitrification), and
474 SOC. Each term was integrated vertically over the whole water column and also over the
475 bottom-most 12 layers and then averaged for the northern and southern regions for each
476 month (Figure 11). We also report these terms for the months during which oxygen
477 decreases (March to August) in Table S2.

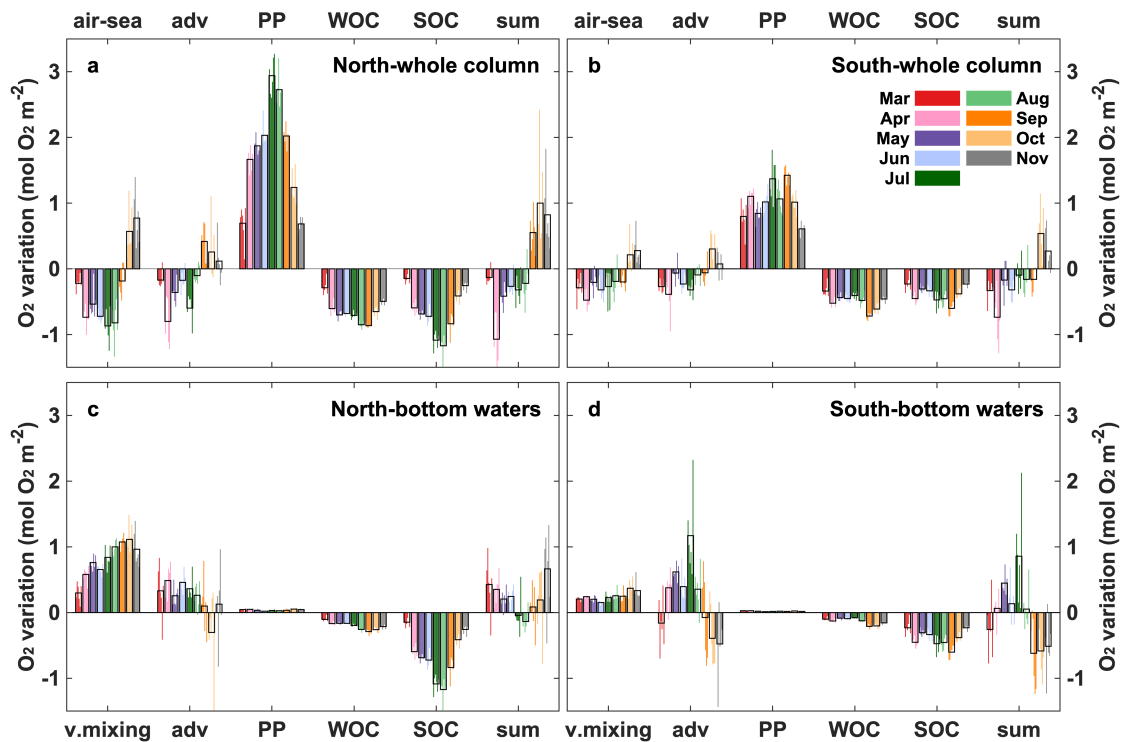


Figure 11. Monthly averaged (2008-2013) oxygen budgets for the whole water column and subsurface water from March to November in the northern and southern hypoxic regions. Adv represents lateral advection and lateral diffusion which is comparatively small, while v.mixing represents vertical turbulent diffusion, which is only relevant for the subsurface budget. Thin color bars represent individual years whereas the black bars are the 6-year average.

478 For the whole water column (Figure 11a, b), biological processes (PP, WOC, and SOC)
 479 greatly exceed physical processes (air-sea exchange and advective transport) in affecting
 480 oxygen. PP is always greater than the sum of WOC and SOC in the whole column
 481 indicating autotrophy in spring and summer. Advection is negative, acting as an oxygen
 482 sink and offsetting 21% of PP on average in the northern and southern regions. Of the two
 483 biological oxygen consumption terms (WOC and SOC), WOC accounts for half of total
 484 respiration. Negative air-sea flux indicates oxygen outgassing into the atmosphere and is
 485 due to photosynthetic oxygen production and decreasing oxygen solubility. However, since
 486 hypoxia only occurs in the subsurface, the subsurface budget below is more instructive.

487 When considering only subsurface waters (Figure 11c, d), the influence of PP decreases
 488 markedly, accounting for less than 2% of that in the whole water column. Vertical turbulent

489 diffusion acts as the largest oxygen source in the subsurface layer. SOC is the dominant
490 oxygen sink accounting for 80% of the total biological oxygen consumption. As
491 photosynthetic oxygen production increases gradually from spring to summer (Figure 12a,
492 b) WOC and SOC also increase as they are closely associated with photosynthetically
493 produced organic matter. Vertical oxygen diffusion tends to covary with PP, implying an
494 oxygen gradient driven by photosynthetic oxygen production in the upper layer. Lateral
495 advection of oxygen is negative in March only (early in the hypoxic season) mainly in the
496 southern region but becomes positive later. This suggests that early in the hypoxic season,
497 import of low-oxygen water contributes to hypoxia generation but advection switches to
498 an oxygen source later. Overall, oxygen sources and sink terms are similar in the northern
499 and southern regions.

500

501 **4. Discussion**

502 We implemented and validated a state-of-the-art physical-biological model for the ECS.
503 The implementation is based on a model that was previously developed and extensively
504 used for the northern Gulf of Mexico (Fennel et al. 2011, Laurent et al. 2012, Yu et
505 al.2015b), a region that is similar to the ECS in that it receives large inputs of FW and
506 nutrients from a major river and develops extensive, annually recurring hypoxia (see Table
507 1 in Fennel and Testa (2019). Our model is more comprehensive than previous models for
508 the ECS.

509 A 6-year simulation was performed and compared to available observations. The model
510 faithfully represents patterns and variability in surface and bottom temperature and salinity,
511 surface chlorophyll and nitrate distributions, bottom oxygen, and correctly simulates the
512 major current patterns in the region (see Section 3.1 and Supplement). We thus deem the
513 model's skill as sufficient for the analysis of biological and physical drivers of hypoxia
514 generation presented here.

515 The model simulates annually recurring hypoxic conditions but with significant
516 interannual and intra-seasonal variability and marked differences in phenology of hypoxic
517 conditions from year to year (Figure 4a, b, c). Interannual variability in hypoxic conditions
518 is much larger than variations in FW input, nutrient load, and bottom oxygen
519 concentrations (Figure 4b) because small variations in oxygen can lead to large changes in

520 hypoxic area when bottom oxygen is near the hypoxic threshold. Interannual variability in
521 hypoxic area is partly explained by variations in annual FW input, consistent with previous
522 studies (Zheng et al., 2016; Zhou et al., 2017). While the correlation between time-
523 integrated hypoxic area and FW input is insignificant, there is a strong and significant
524 negative correlation between mean bottom oxygen in August and annual FW input (Figure
525 5). Annual FW input is also correlated strongly and significantly with the annually
526 integrated spatial extent of the FW plume, which is a useful metric for extent of the region
527 directly influenced by riverine inputs which induce strong density stratification and high
528 productivity.

529 Surprisingly, DIN load is not correlated with FW input, hypoxic area, and mean bottom
530 oxygen in August (Figure 5). This is in contrast to the northern Gulf of Mexico where DIN
531 load is highly correlated with both FW input and nutrient load and frequently used as a
532 predictor of hypoxic extent (Scavia et al. 2017; Laurent and Fennel 2019). However, the
533 lack of correlation between hypoxia and DIN load in the ECS should not be interpreted as
534 biological processes being unimportant in hypoxia generation, just that variations in DIN
535 load do not explain year-to-year differences. In fact, hypoxic area and biological rates (i.e.
536 mean August PP, OC, and SOC) are strongly and significantly correlated (Figure 5),
537 emphasizing the dominant role of biological oxygen consumption. The fact that riverine
538 variations in DIN load do not seem to have an effect suggests that riverine nutrient inputs
539 are large enough to saturate the region with nutrients, similar to the northern Gulf of
540 Mexico where small reductions in nutrient load have a relatively small effect (Fennel and
541 Laurent 2018).

542 Variations in riverine FW input only partly explain interannual variations in hypoxia.
543 For example, the years 2010 and 2012 had similar FW inputs and DIN loads but the hypoxic
544 area was 4 times larger in 2010 than 2012 (Figure 5a). Similarly, 2009 and 2013 had the
545 same FW inputs and nutrient loads but 2009 experienced extensive hypoxia while there
546 was almost none in 2013. In order to elucidate these differences, we investigated biological
547 and physical drivers of intra-seasonal variability.

548 In the ECS, two distinct zones of low oxygen have been observed (Li et al., 2002; Wei
549 et al., 2007; Zhu et al., 2016, 2011). The model simulates these two zones, referred to as
550 the northern and southern zones, consistent with observations (Figure 4d) and with

551 generally higher PP and SOC in the northern zone (Figure 6). Because of these differences
552 we treated the two zones separately in our analysis of intra-seasonal drivers.

553 We found daily biological rates (i.e. PP, OC, SOC) to be significantly correlated with
554 bottom oxygen in both zones, but with relatively large variability around the best linear fit
555 (Figure 7). The biological rates and bottom oxygen are also significantly correlated with
556 the extent of the FW plume (Table 1). Again, these results emphasize the dominant role of
557 biological oxygen consumption, and its relation to riverine inputs, in hypoxia generation
558 but leave a significant fraction of the variability unexplained.

559 Intra-seasonal variability in hypoxic conditions is significantly related to the extent of
560 the FW plume which is partly explained by variations in riverine FW input but strongly
561 modulated by coastal circulation and mixing. Their influence is elucidated by our analysis
562 of the effects of wind direction and strength on hypoxia. Wind direction has a notable effect
563 on the geographic distribution of hypoxia. Southerly, upwelling-favorable winds lead to a
564 more widespread eastward extension of the FW plume with elevated PP and vertical
565 density stratification (Figure 8). Northerly, downwelling-favorable winds create a coastally
566 trapped southward jet that moves FW southward and constrains the plume close to the coast.
567 A similar behavior has been described for the northern Gulf of Mexico (Feng et al., 2014).

568 Wind strength turned out to be one of the dominant factors in hypoxia evolution. We
569 identified high-wind events and showed that whenever bottom oxygen is low, a high-wind
570 event will lead to a partial reoxygenation of bottom waters and decrease hypoxic extent
571 (Figure 9). The impact of high-wind events is also visible in the extent of the FW plume,
572 which is drastically reduced during high winds because FW is mixed. The frequency of
573 high-wind events during summer explains the differences in hypoxic area between 2010
574 and 2012 (Figure 10) and 2009 and 2013 (Figure S8). In 2009 and 2010 there were only
575 few high-wind events during summer while 2012 and 2013 experienced a sequence of
576 storms that led to partial reoxygenation of the water column throughout the summer and
577 thus impeded the development hypoxia.

578 We calculated oxygen budgets for the northern and southern regions considering the
579 whole water-column and the near-bottom layer only. The subsurface budget is particularly
580 useful in providing insights into when and where lateral advection amplifies or mitigates
581 hypoxia and illustrates that SOC is the dominant oxygen sink in the subsurface. The relative

582 importance of WOC and SOC had not previously been quantified for this region due to
583 lack of concurrent WOC and SOC observations and lack of models that realistically
584 account for both processes. The budget for the whole water column is less useful because
585 it is dominated by the oxygen sources, sinks and transport in the surface layer, which does
586 not experience hypoxia and thus is not relevant.

587 The importance of SOC in our model is consistent with recent observational studies in
588 the ECS. SOC on the coastal shelves in the Yellow Sea and ECS has been estimated to
589 range from 1.7 to 17.6 mmol O₂ m⁻² d⁻¹ (mean rate of 7.2 mmol O₂ m⁻² d⁻¹) from April to
590 October except August by Song et al. (2016), and from 9.1 to 62.5 mmol O₂ m⁻² d⁻¹ (mean
591 of 22.6 ± 16.4 mmol O₂ m⁻² d⁻¹) from June to October in Zhang et al. (2017). Simulated
592 SOC in the typical low-oxygen zone falls within the range observed by Zhang et al. (2017)
593 with a mean rate of 20.6 ± 19.2 mmol O₂ m⁻² d⁻¹ between April and October. Based on
594 observations, Zhang et al. (2017) already suggested that SOC is a major contributor to
595 hypoxia formation in below-pycnocline waters, which is further corroborated by our model
596 results. It is also consistent with the modelling study of Zhou et al. (2017), who did not
597 include SOC in the baseline version of their model but showed in a sensitivity study that
598 inclusion of SOC simulates hypoxic extent more realistically. Our results are in line with
599 findings from the northern Gulf of Mexico hypoxic zone where WOC is much larger than
600 SOC below the pycnocline, while SOC is dominant in the bottom 5 m where hypoxia
601 occurs most frequently in summer (Quiñones-Rivera et al., 2007; Yu et al., 2015b).

602 The finding that lateral oxygen transport can act as a net source to subsurface water is
603 also new. On seasonal scales, oxygen advection in the subsurface varies from an oxygen
604 sink in spring to a source in summer, especially in the southern hypoxic region, implying
605 that the TWC becomes an oxygen source when oxygen is depleted in the hypoxic region.
606 This aspect was neglected in previous studies which only emphasized the role of advection
607 as an oxygen sink promoting hypoxia formation (Ning et al., 2011; Qian et al., 2015). The
608 Taiwan Warm Current originates from the subsurface of the Kuroshio northeast to Taiwan
609 Island, and thus represents an intrusion onto the continental shelves from the open ocean
610 (Guo et al., 2006). In addition to oxygen advection, nutrients are transported supporting PP
611 on the ECS shelves (Zhao & Guo, 2011; Grosse et al., 2020). The intrusion of the Taiwan
612 Warm Current and the Kuroshio accompanied by relatively cold and saline water, and

613 nutrient and oxygen transport, is thought to influence hypoxia development (Li et al., 2002;
614 Wang, 2009; Zhou et al., 2017) but no quantification of the relative importance has
615 occurred until now (see companion paper by Grosse et al., 2020, using the same model).

616

617 **5. Conclusions**

618 In this study, a new 3D coupled physical-biological model for the ECS was presented
619 and used to explore the spatial and temporal evolution of hypoxia off the CE and to quantify
620 the major processes controlling interannual and intra-seasonal oxygen dynamics.
621 Validation shows that the model reproduces the observed spatial distribution and temporal
622 evolution of physical and biological variables well.

623 A 6-year simulation with realistic forcing produced large interannual and intra-seasonal
624 variability in hypoxic extent despite relatively modest variations in FW input and nutrient
625 loads. The interannual variations are partly explained by variations in FW input but not
626 DIN load. Nevertheless, elevated rates of biological oxygen consumption are of paramount
627 importance for hypoxia generation in this region, as shown by the high correlation between
628 hypoxic area, bottom oxygen, and biological rates (PP, OC, SOC) on both annual and
629 shorter time scales.

630 Other important explanatory variables of variability in hypoxia are wind direction and
631 strength. Wind direction affects the magnitude of PP and the spatial extent of the FW plume,
632 because southerly, upwelling favorable winds tend to spread the plume over a large area
633 while northerly, downwelling-favorable winds push the plume against the coast and induce
634 a coastal current that contains the FW and moves it downcoast. Wind strength is important
635 because high-wind events lead to a partial reoxygenation whenever bottom oxygen is low
636 and can dramatically decrease the extent of the FW plume. The frequency of high-wind
637 events explains some of the interannual differences in hypoxia, where years with similar
638 FW input, nutrient load, and mean rates of oxygen consumption have display very different
639 hypoxic extents because high-wind events lead to partial reoxygenation of bottom waters.

640 A model-derived oxygen budget shows that SOC is larger than WOC in the subsurface
641 of the hypoxic region. Lateral advection of oxygen in the subsurface switches from an
642 oxygen sink in spring to a source in summer especially in the southern region and is likely

643 associated with open-ocean intrusions onto the coastal shelf supplied by the Taiwan Warm
644 Current.

645 **Acknowledgments:** HZ was supported by the National Key Research and Development
646 Program of China (2016YFC1401602 and 2017YFC1404403) and the China Scholarship
647 Council (CSC). The authors thank the crew of the Dongfanghong2 for providing much help
648 during the sampling cruises, and Compute Canada for access to supercomputer time. KF
649 acknowledges support from the NSERC Discovery Program.

650 **Code/Data Availability:** The ROMS model code is available at <http://myroms.org>.
651 NOAA AVHRR and MODIS-Terra are available at
652 <https://www.nodc.noaa.gov/SatelliteData/ghrsst/> and <http://oceancolor.gsfc.nasa.gov/>.
653 The model results are available on request to the authors.

654 **Author Contributions:** The manuscript is based on HZ's PhD thesis (in Chinese). CB
655 implemented the physical model. HZ added the biological component, performed model
656 simulations, and wrote the first version of the manuscript with input from KF and AL. For
657 the manuscript revision, AL reran the model simulation, AL and KF performed additional
658 analyses, and KF revised the text with input from all co-authors.

659 **Competing Interests:** The authors declare they have no competing interests.

660

661 **References**

- 662 Baird, D., Christian, R. R., Peterson, C. H., & Johnson, G. A.: Consequences of hypoxia on
663 estuarine ecosystem function: Energy diversion from consumers to microbes. *Ecological*
664 *Applications*, 14(3), 805–822. <https://doi.org/10.1890/02-5094>, 2004.
- 665 Bian, C., Jiang, W., & Greatbatch, R. J.: An exploratory model study of sediment transport
666 sources and deposits in the Bohai Sea, Yellow Sea, and East China Sea. *Journal of Geophysical*
667 *Research: Oceans*, 118(11), 5908–5923. <https://doi.org/10.1002/2013JC009116>, 2013a.
- 668 Bian, C., Jiang, W., Quan, Q., Wang, T., Greatbatch, R. J., & Li, W.: Distributions of suspended
669 sediment concentration in the Yellow Sea and the East China Sea based on field surveys during
670 the four seasons of 2011. *Journal of Marine Systems*, 121–122, 24–35,
671 <https://doi.org/10.1016/j.jmarsys.2013.03.013>, 2013b.
- 672 Bianchi, T. S., DiMarco, S. F., Cowan, J. H., Hetland, R. D., Chapman, P., Day, J. W., & Allison,
673 M. A.: The science of hypoxia in the northern Gulf of Mexico: A review. *Science of the Total*
674 *Environment*, 408(7), 1471–1484. <https://doi.org/10.1016/j.scitotenv.2009.11.047>, 2010.

675 Bishop, M. J., Powers, S. P., Porter, H. J., & Peterson, C. H.: Benthic biological effects of
676 seasonal hypoxia in a eutrophic estuary predate rapid coastal development. *Estuarine, Coastal
677 and Shelf Science*, 70(3), 415–422. <https://doi.org/10.1016/j.ecss.2006.06.031>, 2006.

678 Capet, A., Beckers, J. M., & Grégoire, M.: Drivers, mechanisms and long-term variability of
679 seasonal hypoxia on the Black Sea northwestern shelf - Is there any recovery after
680 eutrophication? *Biogeosciences*, 10(6), 3943–3962. <https://doi.org/10.5194/bg-10-3943-2013>,
681 2013.

682 Carton, J. A., & Giese, B. S.: A Reanalysis of Ocean Climate Using Simple Ocean Data
683 Assimilation (SODA). *Monthly Weather Review*, 136(8), 2999–3017,
684 <https://doi.org/10.1175/2007MWR1978.1>, 2008.

685 Chen, C. C., Gong, G. C., & Shiah, F. K., Hypoxia in the East China Sea: One of the largest
686 coastal low-oxygen areas in the world. *Marine Environmental Research*, 64(4), 399–408.
687 <https://doi.org/10.1016/j.marenvres.2007.01.007>, 2007.

688 Chen, J., Cui, T., Ishizaka, J., & Lin, C.: A neural network model for remote sensing of diffuse
689 attenuation coefficient in global oceanic and coastal waters: Exemplifying the applicability of
690 the model to the coastal regions in Eastern China Seas. *Remote Sensing of Environment*, 148,
691 168–177. <https://doi.org/10.1016/j.rse.2014.02.019>, 2014.

692 Chen, X., Shen, Z., Li, Y., & Yang, Y.: Physical controls of hypoxia in waters adjacent to the
693 Yangtze Estuary: A numerical modeling study. *Marine Pollution Bulletin*, 97(1–2), 349–364.
694 <https://doi.org/10.1016/j.marpolbul.2015.05.067>, 2015a.

695 Chen, X., Shen, Z., Li, Y., & Yang, Y.: Tidal modulation of the hypoxia adjacent to the Yangtze
696 Estuary in summer. *Marine Pollution Bulletin*, 100(1), 453–463,
697 <https://doi.org/10.1016/j.marpolbul.2015.08.005>, 2015b.

698 Dee, D. P., Uppala, S. M., Simmons, A. J., Berrisford, P., Poli, P., Kobayashi, S., ... Vitart, F.:
699 The ERA-Interim reanalysis: Configuration and performance of the data assimilation system.
700 *Quarterly Journal of the Royal Meteorological Society*, 137(656), 553–597.
701 <https://doi.org/10.1002/qj.828>, 2011.

702 Diaz, R. J., & Rosenberg, R.: Spreading dead zones and consequences for marine ecosystems.
703 *Science*, 321(5891), 926–929. <https://doi.org/10.1126/science.1156401>, 2008.

704 Egbert, G. D., & Erofeeva, S. Y.: Efficient inverse modeling of barotropic ocean tides. *Journal of*
705 *Atmospheric and Oceanic Technology*, 19(2), 183–204. [https://doi.org/10.1175/1520-0426\(2002\)019<0183:EIMOBO>2.0.CO;2](https://doi.org/10.1175/1520-0426(2002)019<0183:EIMOBO>2.0.CO;2), 2002.

707 Feng, Y., Fennel, K., Jackson, G.A., DiMarco, S.F. & Hetland, R.D.: A model study of the
708 response of hypoxia to upwelling favorable wind on the northern Gulf of Mexico shelf, *Journal*
709 *of Marine Systems* 131, 63-73, 2014.

710 Fennel, K., and Testa, J.M.: Biogeochemical controls on coastal hypoxia, *Annual Review of*
711 *Marine Science*, 11, 105-130, <https://doi.org/10.1146/annurev-marine-010318-095138>, 2019.

712 Fennel, K. and Laurent, A.: N and P as ultimate and proximate limiting nutrients in the northern
713 Gulf of Mexico: implications for hypoxia reduction strategies, *Biogeosciences*, 15, 3121-3131,
714 <https://doi.org/10.5194/bg-15-3121-2018>, 2018.

715 Fennel, K., Hetland, R., Feng, Y., & DiMarco, S.: A coupled physical-biological model of the
716 Northern Gulf of Mexico shelf: Model description, validation and analysis of phytoplankton
717 variability. *Biogeosciences*, 8(7), 1881–1899. <https://doi.org/10.5194/bg-8-1881-2011>, 2011.

718 Fennel, K., Hu, J., Laurent, A., Marta-Almeida, M., & Hetland, R.: Sensitivity of hypoxia
719 predictions for the northern Gulf of Mexico to sediment oxygen consumption and model
720 nesting. *Journal of Geophysical Research: Oceans*, 118(2), 990–1002.
721 <https://doi.org/10.1002/jgrc.20077>, 2013.

722 Fennel, K., Wilkin, J., Levin, J., Moisan, J., O'Reilly, J., & Haidvogel, D.: Nitrogen cycling in
723 the Middle Atlantic Bight: Results from a three-dimensional model and implications for the
724 North Atlantic nitrogen budget. *Global Biogeochemical Cycles*, 20(3), 1–14.
725 <https://doi.org/10.1029/2005GB002456>, 2006.

726 Garcia, H. E., Boyer, T. P., Locarnini, R. A., Antonov, J. I., Mishonov, A. V., Baranova, O. K., ...
727 Johnson, D. R.: *World Ocean Atlas 2013. Volume 3: dissolved oxygen, apparent oxygen*
728 *utilization, and oxygen saturation. NOAA Atlas NESDIS 75*, 2013a.

729 Garcia, H. E., Locarnini, R. A., Boyer, T. P., Antonov, J. I., Baranova, O. K., Zweng, M. M., ...
730 Johnson, D. R.: *World Ocean Atlas 2013, Volume 4 : Dissolved Inorganic Nutrients*
731 *(phosphate, nitrate, silicate). NOAA Atlas NESDIS 76 (Vol. 4)*, 2013b.

732 Grosse, F., Fennel, K., Zhang, H., Laurent, A.: Quantifying the contributions of riverine vs.
733 oceanic nitrogen to hypoxia in the East China Sea, *Biogeosciences*, [https://doi.org/10.5194/bg-](https://doi.org/10.5194/bg-2019-342)
734 [2019-342](https://doi.org/10.5194/bg-2019-342), accepted for publication

735 Guo, J. S., X. M. Hu and Y. L. Yuan: A diagnostic analysis of variations in volume transport
736 through the Taiwan Strait using satellite altimeter data, *Advances in Marine Science*, 23(1):
737 20 – 26 (in Chinese with English abstract), 2005.

738 Haidvogel, D. B., Arango, H., Budgell, W. P., Cornuelle, B. D., Curchitser, E., Di Lorenzo, E., ...
739 Wilkin, J., *Ocean forecasting in terrain-following coordinates: Formulation and skill*

740 assessment of the Regional Ocean Modeling System. *Journal of Computational Physics*,
741 227(7), 3595–3624. <https://doi.org/10.1016/j.jcp.2007.06.016>, 2008.

742 Laurent, A., & Fennel, K.: Simulated reduction of hypoxia in the northern Gulf of Mexico due to
743 phosphorus limitation. *Elementa: Science of the Anthropocene*, 2(1), 000022.
744 <https://doi.org/10.12952/journal.elementa.000022>, 2014.

745 Laurent, A., Fennel, K.: Time-evolving, spatially explicit forecasts of the northern Gulf of
746 Mexico hypoxic zone. *Environmental Science & Technology*, 53, 14,449–14,458, doi:
747 10.1021/acs.est.9b05790, 2019.

748 Laurent, A., Fennel, K., Hu, J., & Hetland, R.: Simulating the effects of phosphorus limitation in
749 the Mississippi and Atchafalaya river plumes. *Biogeosciences*, 9(11), 4707–4723.
750 <https://doi.org/10.5194/bg-9-4707-2012>, 2012.

751 Laurent, A., Fennel, K., Cai, W.-J., Huang, W.-J., Barbero, L., Wanninkhof, R.: Eutrophication-
752 Induced Acidification of Coastal Waters in the Northern Gulf of Mexico: Insights into Origin
753 and Processes from a Coupled Physical-Biogeochemical Model. *Geophys. Res. Lett.*, 44 (2),
754 946–956. <https://doi.org/10.1002/2016GL071881>, 2017.

755 Li, D., Zhang, J., Huang, D., Wu, Y., & Liang, J.: Oxygen depletion off the Changjiang (Yangtze
756 River) Estuary. *Science in China Series D: Earth Science*, 45(12), 1137.
757 <https://doi.org/10.1360/02yd9110>, 2002.

758 Li, H. M., Tang, H. J., Shi, X. Y., Zhang, C. S., & Wang, X. L.: Increased nutrient loads from the
759 Changjiang (Yangtze) River have led to increased Harmful Algal Blooms. *Harmful Algae*, 39,
760 92–101. <https://doi.org/10.1016/j.hal.2014.07.002>, 2014.

761 Li, M., Lee, Y. J., Testa, J. M., Li, Y., Ni, W., Kemp, W. M., & Di Toro, D. M.: What drives
762 interannual variability of hypoxia in Chesapeake Bay: Climate forcing versus nutrient loading?
763 *Geophysical Research Letters*, 43(5), 2127–2134. <https://doi.org/10.1002/2015GL067334>,
764 2016.

765 Li, X., Bianchi, T. S., Yang, Z., Osterman, L. E., Allison, M. A., DiMarco, S. F., & Yang, G.:
766 Historical trends of hypoxia in Changjiang River estuary: Applications of chemical biomarkers
767 and microfossils. *Journal of Marine Systems*, 86(3–4), 57–68, 2011.
768 <https://doi.org/10.1016/j.jmarsys.2011.02.003>

769 Liu, K. K., Yan, W., Lee, H. J., Chao, S. Y., Gong, G. C., & Yeh, T. Y.: Impacts of increasing
770 dissolved inorganic nitrogen discharged from Changjiang on primary production and seafloor
771 oxygen demand in the East China Sea from 1970 to 2002. *Journal of Marine Systems*, 141,
772 200–217. <https://doi.org/10.1016/j.jmarsys.2014.07.022>, 2015.

773 Liu, S. M., Hong, G.-H., Ye, X. W., Zhang, J., & Jiang, X. L.: Nutrient budgets for large Chinese
774 estuaries and embayment. *Biogeosciences Discussions*, 6(1), 391–435.
775 <https://doi.org/10.5194/bgd-6-391-2009>, 2009.

776 Liu, S. M., Zhang, J., Chen, H. T., Wu, Y., Xiong, H., & Zhang, Z. F.: Nutrients in the
777 Changjiang and its tributaries. *Biogeochemistry*, 62(1), 1–18, 2003.

778 Locarnini, R. A., Mishonov, A. V., Antonov, J. I., Boyer, T. P., Garcia, H. E., Baranova, O.
779 K., ... Seidov, D.: World Ocean Atlas 2013. Vol. 1: Temperature. S. Levitus, Ed.; A.
780 Mishonov, Technical Ed.; NOAA Atlas NESDIS, 73, 40. [https://doi.org/10.1182/blood-2011-
781 06-357442](https://doi.org/10.1182/blood-2011-06-357442), 2013.

782 Ni, X., Huang, D., Zeng, D., Zhang, T., Li, H., & Chen, J.: The impact of wind mixing on the
783 variation of bottom dissolved oxygen off the Changjiang Estuary during summer. *Journal of*
784 *Marine Systems*, 154, 122–130. <https://doi.org/10.1016/j.jmarsys.2014.11.010>, 2016.

785 Ning, X., Lin, C., Su, J., Liu, C., Hao, Q., & Le, F.: Long-term changes of dissolved oxygen,
786 hypoxia, and the responses of the ecosystems in the East China Sea from 1975 to 1995. *Journal*
787 *of Oceanography*, 67(1), 59–75. <https://doi.org/10.1007/s10872-011-0006-7>, 2011.

788 Peña, A., Katsev, S., Oguz, T., & Gilbert, D.: Modeling dissolved oxygen dynamics and hypoxia.
789 *Biogeosciences*, 7(3), 933–957. <https://doi.org/10.5194/bg-7-933-2010>, 2010.

790 Qian, W., Dai, M., Xu, M., Kao, S. ji, Du, C., Liu, J., ... Wang, L.: Non-local drivers of the
791 summer hypoxia in the East China Sea off the Changjiang Estuary. *Estuarine, Coastal and*
792 *Shelf Science*, 1–7. <https://doi.org/10.1016/j.ecss.2016.08.032>, 2015.

793 Quiñones-Rivera, Z. J., Wissel, B., Justić, D., & Fry, B.: Partitioning oxygen sources and sinks in
794 a stratified, eutrophic coastal ecosystem using stable oxygen isotopes. *Marine Ecology*
795 *Progress Series*, 342, 69–83. <https://doi.org/10.3354/meps342069>, 2007.

796 Rabalais, N. N., Díaz, R. J., Levin, L. A., Turner, R. E., Gilbert, D., & Zhang, J.: Dynamics and
797 distribution of natural and human-caused hypoxia. *Biogeosciences*, 7, 585–619.
798 <https://doi.org/10.5194/bg-7-585-2010>, 2010.

799 Scavia, D., Bertani, I., Obenour, D. R., Turner, R. E., Forrest, D. R. & Katin, A.: Ensemble
800 modeling informs hypoxia management in the northern Gulf of Mexico, *P. Natl. Acad. Sci.*
801 *USA*, 114, 8823–8828, 2017.

802 Scully, M. E.: Physical controls on hypoxia in Chesapeake Bay: A numerical modeling study.
803 *Journal of Geophysical Research: Oceans*, 118(3), 1239–1256,
804 <https://doi.org/10.1002/jgrc.20138>, 2013.

805 Smolarkiewicz, P. K., & Margolin, L. G.: MPDATA: A finite-difference solver for geophysical
806 flows. *Journal of Computational Physics*, 140, 459–480, 1998.

807 Song, G., Liu, S., Zhu, Z., Zhai, W., Zhu, C., & Zhang, J.: Sediment oxygen consumption and
808 benthic organic carbon mineralization on the continental shelves of the East China Sea and the
809 Yellow Sea. *Deep-Sea Research Part II: Topical Studies in Oceanography*, *124*, 53–63.
810 <https://doi.org/10.1016/j.dsr2.2015.04.012>, 2016.

811 Tong, Y., Zhao, Y., Zhen, G., Chi, J., Liu, X., Lu, Y., ... Zhang, W.: Nutrient Loads Flowing into
812 Coastal Waters from the Main Rivers of China (2006–2012). *Scientific Reports*, *5*, 16678.
813 <https://doi.org/10.1038/srep16678>, 2015.

814 Umlauf, L., & Burchard, H.: A generic length-scale equation for geophysical. *Journal of Marine*
815 *Research*, *61*(2), 235–265. <https://doi.org/10.1357/002224003322005087>, 2003.

816 Wang, B.: Hydromorphological mechanisms leading to hypoxia off the Changjiang estuary.
817 *Marine Environmental Research*, *67*(1), 53–58,
818 <https://doi.org/10.1016/j.marenvres.2008.11.001>, 2009.

819 Wang, B., Wei, Q., Chen, J., & Xie, L.: Annual cycle of hypoxia off the Changjiang (Yangtze
820 River) Estuary. *Marine Environmental Research*, *77*, 1–5,
821 <https://doi.org/10.1016/j.marenvres.2011.12.007>, 2012.

822 Wang, B., Chen, J., Jin, H., Li, H., Huang, D., & Cai, W.-J.: Diatom bloom-derived bottom water
823 hypoxia off the Changjiang Estuary, with and without typhoon influence, *Limnology and*
824 *Oceanography*, *62*, 1552–1569, <https://doi.org/10.1002/lno.10517>, 2017.

825 Wang, H., Dai, M., Liu, J., Kao, S. J., Zhang, C., Cai, W. J., ... Sun, Z.: Eutrophication-Driven
826 Hypoxia in the East China Sea off the Changjiang Estuary. *Environmental Science and*
827 *Technology*, *50*(5), 2255–2263. <https://doi.org/10.1021/acs.est.5b06211>, 2016.

828 Wang, J., Yan, W., Chen, N., Li, X., & Liu, L.: Modeled long-term changes of DIN:DIP ratio in
829 the Changjiang River in relation to Chl- α and DO concentrations in adjacent estuary. *Estuarine,*
830 *Coastal and Shelf Science*, *166*, 153–160. <https://doi.org/10.1016/j.ecss.2014.11.028>, 2015.

831 Wei, H., He, Y., Li, Q., Liu, Z., & Wang, H.: Summer hypoxia adjacent to the Changjiang
832 Estuary. *Journal of Marine Systems*, *67*(3–4), 292–303,
833 <https://doi.org/10.1016/j.jmarsys.2006.04.014>, 2007.

834 Wei, H., Luo, X., Zhao, Y., & Zhao, L.: Intraseasonal variation in the salinity of the Yellow and
835 East China Seas in the summers of 2011, 2012, and 2013. *Hydrobiologia*, *754*(1), 13–28.
836 <https://doi.org/10.1007/s10750-014-2133-9>, 2015.

837 Wu, R. S. S.: Hypoxia: From molecular responses to ecosystem responses. *Marine Pollution*
838 *Bulletin*, *45*(1–12), 35–45. [https://doi.org/10.1016/S0025-326X\(02\)00061-9](https://doi.org/10.1016/S0025-326X(02)00061-9), 2002.

839 Yu, L., Fennel, K., & Laurent, A.: A modeling study of physical controls on hypoxia generation
840 in the northern Gulf of Mexico. *Journal of Geophysical Research C: Oceans*, *120*(7), 5019–
841 5039. <https://doi.org/10.1002/2014JC010634>, 2015a.

842 Yu, L., Fennel, K., Laurent, A., Murrell, M. C., & Lehrter, J. C.: Numerical analysis of the
843 primary processes controlling oxygen dynamics on the Louisiana shelf. *Biogeosciences*, *12*(7),
844 2063–2076. <https://doi.org/10.5194/bg-12-2063-2015>, 2015b.

845 Yuan, D., Zhu, J., Li, C., & Hu, D.: Cross-shelf circulation in the Yellow and East China Seas
846 indicated by MODIS satellite observations. *Journal of Marine Systems*, *70*(1–2), 134–149.
847 <https://doi.org/10.1016/j.jmarsys.2007.04.002>, 2008.

848 Zhang, H., Zhao, L., Sun, Y., Wang, J., & Wei, H.: Contribution of sediment oxygen demand to
849 hypoxia development off the Changjiang Estuary. *Estuarine, Coastal and Shelf Science*, *192*,
850 149–157. <https://doi.org/10.1016/j.ecss.2017.05.006>, 2017.

851 Zhang, J.: Nutrient elements in large Chinese estuaries. *Continental Shelf Research*, *16*(8), 1023–
852 1045. [https://doi.org/10.1016/0278-4343\(95\)00055-0](https://doi.org/10.1016/0278-4343(95)00055-0), 1996.

853 Zhao, L., & Guo, X.: Influence of cross-shelf water transport on nutrients and phytoplankton in
854 the East China Sea: A model study. *Ocean Science*, *7*(1), 27–43. [https://doi.org/10.5194/os-7-](https://doi.org/10.5194/os-7-27-2011)
855 [27-2011](https://doi.org/10.5194/os-7-27-2011), 2011.

856 Zheng, J., Gao, S., Liu, G., Wang, H., & Zhu, X.: Modeling the impact of river discharge and
857 wind on the hypoxia off Yangtze Estuary. *Natural Hazards and Earth System Sciences*, *16*(12),
858 2559–2576. <https://doi.org/10.5194/nhess-16-2559-2016>, 2016.

859 Zhou, F., Chai, F., Huang, D., Xue, H., Chen, J., Xiu, P., ... Wang, K.: Investigation of hypoxia
860 off the Changjiang Estuary using a coupled model of ROMS-CoSiNE. *Progress in*
861 *Oceanography*, *159*, 237–254. <https://doi.org/10.1016/j.pocean.2017.10.008>, 2017.

862 Zhou, F., Huang, D., Ni, X., Xuan, J., Zhang, J., & Zhu, K.: Hydrographic analysis on the multi-
863 time scale variability of hypoxia adjacent to the Changjiang River Estuary. *Shengtai Xuebao/*
864 *Acta Ecologica Sinica*, *30*(17), 4728–4740, 2010.

865 Zhu, J., Zhu, Z., Lin, J., Wu, H., & Zhang, J.: Distribution of hypoxia and pycnocline off the
866 Changjiang Estuary, China. *Journal of Marine Systems*, *154*, 28–40.
867 <https://doi.org/10.1016/j.jmarsys.2015.05.002>, 2016.

868 Zhu, Z.-Y., Zhang, J., Wu, Y., Zhang, Y.-Y., Lin, J., & Liu, S.-M.: Hypoxia off the Changjiang
869 (Yangtze River) Estuary: Oxygen depletion and organic matter decomposition. *Marine*
870 *Chemistry*, *125*(1–4), 108–116. <https://doi.org/10.1016/j.marchem.2011.03.005>, 2011.

871 Zweng, M. M., Reagan, J. R., Antonov, J. I., Mishonov, A. V., Boyer, T. P., Garcia, H. E., ...
872 Bidlle, M. M., World Ocean Atlas 2013, Volume 2: Salinity. NOAA Atlas NESDIS (Vol. 119).
873 <https://doi.org/10.1182/blood-2011-06-357442>, 2013.
874